Journal of Experimental and Theoretical Physics, Vol. 91, No. 2, 2000, pp. 369–383.
Translated from Zhurnal Éksperimental'noĭ i Teoreticheskoĭ Fiziki, Vol. 118, No. 2, 2000, pp. 422–437.

SOLIDS
Electronic Properties

Evolution of the Band Structure of Quasiparticles with Doping in Copper Oxides on the Basis of a Generalized Tight-Binding Method

V. A. Gavrichkov*, S. G. Ovchinnikov, A. A. Borisov, and E. G. Goryachev

Kirenskii Institute of Physics, Siberian Division, Russian Academy of Sciences, Krasnoyarsk, 660036 Russia
**e-mail: gav@ksc.krasn.ru*

Received January 18, 2000

Abstract—Two methods for stabilizing the two-hole $^3B_{1g}$ state as the ground state instead of the Zhang–Rice singlet are determined on the basis of an orthogonal cellular basis for a realistic multiband *pd* model of a CuO_2 layer and the dispersion relations for the valence band top in undoped and doped cases are calculated. In the undoped case, aside from the valence band, qualitatively corresponding to the experimental ARPES data for $Sr_2CuO_2Cl_2$ and the results obtained on the basis of the *t*–*t*'–*J* model, the calculations give a zero-dispersion virtual level at the valence band top itself. Because of the zero amplitude of transitions forming the virtual level the response corresponding to it is absent in the spectral density function. In consequence, the experimental ARPES data do not reproduce its presence in this antiferromagnetic undoped dielectric. A calculation of the doped case showed that the virtual level transforms into an impurity-type band and acquires dispersion on account of the nonzero occupation number of the two-hole states and therefore should be detected in ARPES experiments as a high-energy peak in the spectral density. The computed dispersion dependence for the valence band top is identical to the dispersion obtained by the Monte Carlo method, and the ARPES data for optimally doped $Bi_2Sr_2CaCu_2O_{8+\delta}$ samples. The data obtained also make it possible to explain the presence of an energy pseudogap at the symmetric *X* point of the Brillouin band of HTSC compounds. © *2000 MAIK "Nauka/Interperiodica".*

1. INTRODUCTION

Intense discussions about the choice of an effective model for describing the physical properties of CuO_2 planes in perovskite structures has been going on since the discovery of high-temperature superconductivity. Suggestions [1] that the single-band Hubbard model could be the key to understanding the nature of the unusual behavior of these materials were made back in 1987. In the strong correlations regime the Hubbard model reduces to the so-called *t*–*J* model with exchange interaction $J = 4t^2/U$, corresponding to second-order of perturbation theory. Following experimental evidence [2, 3] showing that the mobile charge carriers are primarily in the $2p_x$ and $2p_y$ orbitals, Emery proposed a three-band generalized Hubbard model [4] (the so-called Emery *p*–*d* model) for describing the electronic structure. In this approach there is no longer any obvious relation to the single-band Hubbard model. Considering the importance of charge-transfer processes, a similar approach was proposed in [5, 6]. Subsequently, Zhang and Rice showed [7] that at least for a strong Coulomb repulsion and high charge transfer energy the Emery model does indeed reduce to an effective single-band model, since the doped hole charge carriers are in a singlet state A_{1g}—the Zhang–Rice singlet state, separated well by an energy gap from the other possible two-hole states. The concept of a Zhang–Rice singlet has been found to be true in principle and productive, even though once again it was based on the perturbation theory for the tight-binding case, where the Coulomb interactions on oxygen, between oxygen and copper, as well as oxygen–oxygen charge transfer were neglected. Eskes and Jefferson demonstrated [8] that this approach is not always correct for realistic values of the model parameters. Nonetheless, calculations in Anderson's impurity model [9] as well as cluster calculations [10, 11] based on a three-band *pd* model indeed confirmed that the Zhang–Rice singlet is well separated in energy from the bulk of the two-hole states. Jefferson, Eskes, and Feiner [12] and, independently, Lovtsov and Yushankhaem [13] as well as Schutler and Fedro [14], using a cluster method of perturbation theory introduced previously by Ovchinnikov, Sandalov [15] and Jefferson [16], have given a more accurate derivation of the single-band model. The most complete derivation of the *t*–*J* model from the three-band *p*–*d* model, using a cluster perturbation theory, is contained in the work of Belinicher, Chernyshov, and Shubin [17]. The investigations have made it clear that hops not only between nearest neighbors, *t* (intersublattice hops), but also between the second neighbors, *t*' (intrasublattice hops), and third neighbors, *t*'', are important for the dispersion law for a hole moving against the background of antiferromagnetic (AFM) spin order. It is the terms *t*' that made it possible to

describe on the basis of the t–t'–J model the dispersion law at the valence band top in $Sr_2CuO_2Cl_2$ [18, 19], obtained experimentally by ARPES spectroscopy [20]. At the same time, there are a number of experimental and theoretical indications showing that the three-band p–d model is itself inadequate. Thus, the absorption spectra of polarized X-rays (XAS) [21] and electronic loss spectra (ELS) [2] have revealed an appreciable (10–15%) population of $d_{3z^2-r^2}$ copper orbitals in all p-type HTSCs. In [23, 24] the effect of Coulomb repulsion on oxygen and between oxygen and copper on the effective interactions in a single-band model was examined, and the main consequences of using a realistic $d_{x^2-y^2}$, $d_{3z^2-r^2}$, p_x, p_y, p_z orbital basis on the possibility of constructing an effective one-band model were indicated. Specifically, when the apical oxygen approaches the CuO_2 plane as the degree of doping increases, the two-hole triplet term $^3B_{1g}$ can compete with the Zhang–Rice singlet. As a result, the systematic description of the physics of the lower-lying excitations is no longer possible in the one-band effective model. A similar conclusion was obtained earlier on the basis of a generalized tight-binding method [15]. In this method all possible multihole terms as well as Coulomb and exchange interactions are taken into account. The method formulated using the equations of motion for the Green's functions makes it possible, in principle, to calculate in a unified approach the dispersion curves and the spectral density of states and their temperature, field, and concentration dependences.

The generalized tight-binding method has been used to calculate the dispersion laws and density of states of an undoped CuO_2 layer in the paramagnetic [25] and antiferromagnetic [26] states. The band structure of the quasiparticles was found to depend on the temperature, magnetic field, and particle density. Specifically, for doping with holes new states, similar to deep impurity levels in doped semiconductors, appear in the semiconductor gap [27, 28]. The results of the calculations of the dispersion law of the valence band top in undoped CuO_2 layer were found to be in good agreement with the experimental ARPES-spectroscopy data for $Sr_2CuO_2Cl_2$ [20]. However, the problem of the common oxygen was solved in [15, 25–28] by artificially dividing the CuO_2 layer into two sublattices with the triplets O–Cu–O as a unit cell in each sublattice. In addition, the unit cell in one of the sublattices is turned by 90° with respect to the unit cell in the other sublattice. Since all Cu–O distances in the planes are the same, there are no reasons for such a separation into two sublattices. It would be more systematic to use CuO_6 (CuO_5) cells and the Shastry canonical-fermion representations [29], as done in [12, 16, 17, 23, 24]. In what follows we shall combine the strong aspects of both methods into a single approach. Specifically, in the present paper a systematic formulation is given for the generalized tight-binding method, where a CuO_6 cluster will serve as the unit cell, and the problem of the nonorthogonality of the molecular orbitals of neighboring clusters will be solved in the obvious manner—by constructing the corresponding Wannier functions on the $d_{x^2-y^2}$, $d_{3z^2-r^2}$, p_x, p_y, p_z five-orbital initial basis of atomic states.

The single-cell part of the Hamiltonian factorizes in the new symmetric basis, making it possible to classify according to symmetry all possible effective single-particle excitations in a CuO_2 plane. A subsequent exact diagonalization of the Hamiltonian of a unit cell and a transition to the Hubbard operator representation make it possible to take account of the part of the Hamiltonian that corresponds to hops. The construction and analysis of the dispersion relations are performed using the generalized tight-binding method and the equations of motion for the corresponding Green's functions. The nature of the states at the valence band top of HTSC compounds and the behavior of the states as a function of temperature and hole density are analyzed in the Conclusions.

2. EFFECTIVE HAMILTONIAN OF A CuO_2 LAYER IN THE CELLULAR REPRESENTATION

The initial Hamiltonian of the model can be written in the standard manner:

$$H = H_d + H_p + H_{pd} + H_{pp}, \quad H_d = \sum_r H_d(r), \quad (1)$$

$$H_d(\mathbf{r}) = \sum_{\lambda\sigma}\Bigg[(\varepsilon_\lambda - \mu)d^+_{\lambda\mathbf{r}\sigma}d_{\lambda\mathbf{r}\sigma} + \frac{1}{2}U_\lambda n^\sigma_{\lambda\mathbf{r}}n^{-\sigma}_{\lambda\mathbf{r}}$$

$$+ \sum_{\lambda'\sigma'}\Bigg(-J_d d^+_{\lambda\mathbf{r}\sigma}d_{\lambda\mathbf{r}\sigma'}d^+_{\lambda'\mathbf{r}\sigma'} + \sum_{\mathbf{r}'}V_{\lambda\lambda'}n^\sigma_{\lambda\mathbf{r}}n^{\sigma'}_{\lambda'\mathbf{r}'}\Bigg)\Bigg],$$

$$H_p = \sum_{\mathbf{i}} H_p(\mathbf{i}),$$

$$H_p(\mathbf{i}) = \sum_{\alpha\sigma}\Bigg[(\varepsilon_\alpha - \mu)p^+_{\alpha\mathbf{i}\sigma}p_{\alpha\mathbf{i}\sigma} + \frac{1}{2}U_\alpha n^\sigma_{\alpha\mathbf{i}}n^{-\sigma}_{\alpha\mathbf{i}}$$

$$+ \sum_{\alpha'\mathbf{i}'\sigma'}V_{\alpha\alpha'}n^\sigma_{\alpha\mathbf{i}}n^{\sigma'}_{\alpha'\mathbf{i}'}\Bigg],$$

$$H_{pd} = \sum_{\langle\mathbf{i},\mathbf{r}\rangle} H_{pd}(\mathbf{i},\mathbf{r}),$$

$$H_{pd}(\mathbf{i},\mathbf{r}) = \sum_{\alpha\lambda\sigma\sigma'}(t_{\lambda\alpha}p^+_{a\mathbf{i}\sigma}d_{\mathbf{r}\lambda\sigma} + V_{\alpha\lambda}n^\sigma_{\alpha\mathbf{i}}n^{\sigma'}_{\lambda\mathbf{r}}),$$

$$H_{pp} = \sum_{\langle\mathbf{i},\mathbf{r}\rangle}\sum_{\alpha\beta\sigma}(t_{\alpha\beta}p^+_{\alpha\mathbf{i}\sigma}p_{\beta\mathbf{j}\sigma} + \text{H.c.}),$$

where

$$n^{\sigma}_{\lambda \mathbf{i}} = d^{+}_{\lambda \mathbf{i}\sigma} d_{\lambda \mathbf{i}\sigma}, \quad n^{\sigma}_{\alpha \mathbf{i}} = p^{+}_{\alpha \mathbf{i}\sigma} p_{\alpha \mathbf{i}\sigma}.$$

The indices **r** and **i** run through the positions $d_{x^2-y^2}$, $d_{3z^2-r^2}$, and p_x, p_y, p_z sets of localized atomic orbitals. Similarly, $\varepsilon_\lambda = \varepsilon_{d_x}$ ($\lambda = d_x$), ε_{d_x} ($\lambda = d_z$) and $\varepsilon_\alpha = \varepsilon_p$ ($\alpha = p_x, p_y$), ε_{p_x} ($\alpha = p_z$) are the energies of the corresponding atomic orbitals; $t_{\lambda\alpha} = t_{pd}$ ($\lambda = d_x$, $\alpha = p_x, p_y$); $t_{pd}/\sqrt{3}$ ($\lambda = d_z$, $\alpha = p_x, p_y$) are the matrix elements of a hop; $U_\lambda = U_d$ ($\lambda = d_x, d_z$) and $U_\alpha = U_p$ ($\alpha = p_x, p_y, p_z$) are intraatomic Coulomb interactions; $V_{\alpha\lambda} = V_{pd}$ ($\alpha = p_x, p_y$; $\lambda = d_x, d_z$) and V'_{pd} ($\alpha = p_z$; $\lambda = d_x, d_y$) are the copper-oxygen Coulomb repulsion energies. All matrix elements of the Coulomb and exchange interactions are assumed to be independent of the form of the *d* or *p* planar orbitals. A prime indicates an interaction with apical oxygen. The first step in converting our Hamiltonian to the cellular basis corresponds to the analogous step in the method of [23] and refers to the transformation of the hopping part of the Hamiltonian.

Depending on the elements between CuO_2 layers, the copper ion can have oxygen coordination 6 in La_2CuO_4 compounds, 1-2-0-1 and 2-2-0-1 (Bi and Tl), 5 in the compounds 1-2-3, 1-2-4, 1-2-1-2, 2-2-1-2 (Bi, Tl), and 4 in the compound Nd_2CuO_4. In what follows we shall work with a CuO_6 cluster as the most general case. All subsequent calculations are also valid, with minimal changes, for smaller coordination numbers. Figure 1 displays the unit cell of the CuO_2 plane with the accompanying apical oxygen. In accordance with the choice of phases in Fig. 1, the part of the Hamiltonian of a CuO_6 cell that takes account of the hops can be written as follows:

$$\begin{aligned} H^{c}_{pd} &= t_{pd} d^{+}_{x}(p_{x-1/2,\sigma} - p_{x+1/2,\sigma} + p_{y-1/2,\sigma} - p_{y+1/2,\sigma}) \\ &+ \frac{t_{pd} d^{+}_{z}}{\sqrt{3}}(-p_{x-1/2,\sigma} + p_{x+1/2,\sigma} + p_{y-1/2,\sigma} - p_{y_{+1/2,\sigma}}) + \text{h.c.}, \\ H^{c}_{pp} &= t_{pp}(p^{+}_{x-1/2,\sigma} p_{y+1/2,\sigma} - p^{+}_{x-1/2,\sigma} p_{y-1/2,\sigma} \\ &- p^{+}_{y+1/2,\sigma} p_{x+1/2,\sigma} + p^{+}_{x+1/2,\sigma} p_{y-1/2,\sigma}) + \text{h.c.} \end{aligned} \tag{2}$$

In the initial reducible representation the choice of phases can be made in any other manner, since the subsequent Fourier- and linear transformations are similar to using the method of projection operators in molecular-orbital theory to construct the functions belonging

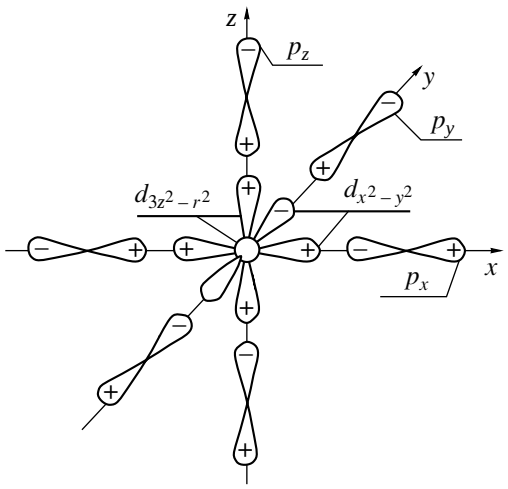

Fig. 1. Unit cell of a CuO_2 layer. The choice of phases corresponds to an initial reducible representation.

to irreducible representations and contained in the initial representation. We shall define the Fourier-transform as follows:

$$\begin{aligned} d_{\lambda \mathbf{k}\sigma} &= \frac{1}{\sqrt{N}} \sum_{\mathbf{f}} d_{\lambda \mathbf{f}\sigma} e^{-i\mathbf{k}\cdot\mathbf{f}}, \\ p_{\alpha \mathbf{k}\sigma} &= \frac{1}{\sqrt{N}} \sum_{\mathbf{m}} p_{\alpha \mathbf{m}\sigma} e^{-i\mathbf{k}\cdot\mathbf{m}}. \end{aligned} \tag{3}$$

Summing over all cells and performing the indicated Fourier transform, we arrive at

$$\begin{aligned} H_{pd} &= t_{pd} \sum_{\mathbf{k}\sigma} d^{+}_{x\mathbf{k}\sigma}(-2i)(s_x p_{x\mathbf{k}\sigma} + s_y p_{y\mathbf{k}\sigma}) \\ &+ \frac{t_{pd}}{\sqrt{3}} \sum_{\mathbf{k}\sigma} d^{+}_{z\mathbf{k}\sigma} 2i(s_x p_{x\mathbf{k}\sigma} - s_y p_{y\mathbf{k}\sigma}) + \text{h.c.}, \\ H_{pp} &= -4t_{pp} \sum_{\mathbf{k}\sigma} s_x s_y p^{+}_{x\mathbf{k}\sigma} p_{y\mathbf{k}\sigma} + \text{h.c.}, \\ s_x &= \sin\frac{k_x}{2}, \quad s_y = \sin\frac{k_y}{2}. \end{aligned} \tag{4}$$

Using the linear transformation $\hat{S}$, we introduce the new operators $a_{\mathbf{k}\sigma}$ and $b_{\mathbf{k}\sigma}$ annihilating a *p* hole in the molecular orbitals of oxygen:

$$\begin{aligned} \begin{pmatrix} b_{\mathbf{k}\sigma} \\ a_{\mathbf{k}\sigma} \end{pmatrix} &= \hat{S} \begin{pmatrix} p_{x\mathbf{k}\sigma} \\ p_{y\mathbf{k}\sigma} \end{pmatrix} \\ &= \begin{pmatrix} is_x/\mu_{\mathbf{k}} & is_y/\mu_{\mathbf{k}} \\ is_y/\mu_{\mathbf{k}} & -is_x/\mu_{\mathbf{k}} \end{pmatrix} \begin{pmatrix} p_{x\mathbf{k}\sigma} \\ p_{y\mathbf{k}\sigma} \end{pmatrix}, \end{aligned} \tag{5}$$

where

$$\mu_{\mathbf{k}}^2 = s_x^2 + s_y^2, \quad |\hat{S}| = 1.$$

The new operators satisfy the required commutation relations $\{b_{\mathbf{k}\sigma}^+, a_{\mathbf{p}\sigma}\} = 0$. Making the substitution

$$p_{x\mathbf{k}\sigma} = -\frac{\mathbf{i}}{\mu_{\mathbf{k}}}(s_x b_{\mathbf{k}\sigma} + s_y a_{\mathbf{k}\sigma}),$$

$$p_{y\mathbf{k}\sigma} = -\frac{\mathbf{i}}{\mu_{\mathbf{k}}}(s_y b_{\mathbf{k}\sigma} - s_x a_{\mathbf{k}\sigma}),$$

we find that H_{pd} and H_{pp} can be written as follows:

$$\begin{aligned} H_{pd} &= -2t_{pd}\sum_{\mathbf{k}\sigma}\mu_{\mathbf{k}} d_{x\mathbf{k}\sigma}^+ b_{\mathbf{k}\sigma} \\ &+ \frac{2t_{pd}}{\sqrt{3}}\sum_{\mathbf{k}\sigma}(\xi_{\mathbf{k}} d_{z\mathbf{k}\sigma}^+ b_{\mathbf{k}\sigma} + \lambda_{\mathbf{k}} d_{z\mathbf{k}\sigma}^+ a_{\mathbf{k}\sigma}) + \text{h.c.} \\ &= -2t_{pd}\sum_{\mathbf{ij}}\mu_{\mathbf{ij}} d_{x\mathbf{i}\sigma}^+ b_{\mathbf{j}\sigma} \\ &+ \frac{2t_{pd}}{\sqrt{3}}\sum_{\mathbf{ij}}(\xi_{\mathbf{ij}} d_{z\mathbf{i}\sigma}^+ b_{\mathbf{j}\sigma} + \lambda_{\mathbf{ij}} d_{z\mathbf{i}\sigma}^+ a_{\mathbf{j}\sigma}) + \text{h.c.}, \\ H_{pp} &= -2t_{pp}\sum_{\mathbf{k}\sigma}\nu_{\mathbf{k}} b_{\mathbf{k}\sigma}^+ b_{\mathbf{k}\sigma} + 2t_{pp}\sum_{\mathbf{k}\sigma}\nu_{\mathbf{k}} a_{\mathbf{k}\sigma}^+ a_{\mathbf{k}\sigma} \\ &- 2t_{pp}\sum_{\mathbf{k}\sigma}\chi_{\mathbf{k}}(b_{\mathbf{k}\sigma}^+ a_{\mathbf{k}\sigma} + \text{h.c.}) \\ &= -2t_{pp}\sum_{\mathbf{ij}\sigma}\nu_{\mathbf{ij}} b_{\mathbf{i}\sigma}^+ b_{\mathbf{j}\sigma} + 2t_{pp}\sum_{\mathbf{ij}\sigma}\nu_{\mathbf{ij}} a_{\mathbf{i}\sigma}^+ a_{\mathbf{j}\sigma} \\ &+ 2t_{pp}\sum_{\mathbf{ij}\sigma}\chi_{\mathbf{ij}}(a_{\mathbf{i}\sigma}^+ b_{\mathbf{j}c} + \text{h.c.}), \end{aligned} \tag{6}$$

where

$$\lambda_{\mathbf{k}} = \frac{2s_x s_y}{\mu_{\mathbf{k}}}, \quad \xi_{\mathbf{k}} = \frac{s_x^2 - s_y^2}{\mu_{\mathbf{k}}},$$

$$\nu_{\mathbf{k}} = \frac{4s_x^2 s_y^2}{\mu_{\mathbf{k}}^2}, \quad \chi_{\mathbf{k}} = \frac{2s_x s_y}{\mu_{\mathbf{k}}^2}(s_x^2 - s_y^2).$$

Inside a cell $\xi_{\mathbf{i}=\mathbf{j}} = 0$ and $\chi_{\mathbf{i}=\mathbf{j}} = 0$ in agreement with the fact that the $b_{\mathbf{k}\sigma}^+|0\rangle$ and $a_{\mathbf{k}\sigma}^+|0\rangle$ states belong to different b_1 and a_1 irreducible representations. Similar transformations for contributions from apical oxygen to the part of the Hamiltonian that takes account of hops,

$$\begin{aligned} H_{pp}^c &= t_{pp}'\{p_{z+1/2,\sigma}^+(p_{x-1/2,\sigma} - p_{x+1/2,\sigma} - p_{y-1/2,\sigma} \\ &+ p_{y+1/2,\sigma}) - p_{z-1/2,\sigma}^+(p_{x-1/2,\sigma} - p_{x+1/2,\sigma} \\ &- p_{y-1/2,\sigma} + p_{y+1/2,\sigma})\} + \text{h.c.}, \\ H_{pd}^{\prime c} &= -\frac{2t_{pd}'}{\sqrt{3}}(p_{z+1/2,\sigma}^+ d_{z\sigma} - p_{z-1/2,\sigma\Sigma}^+ d_{z\sigma} + \text{h.c.}), \end{aligned} \tag{7}$$

lead to the following result:

$$\begin{aligned} H_{pp}' &= -2t_{pp}'\sum_{\mathbf{k}\sigma}(\xi_{\mathbf{k}\sigma} p_{z\mathbf{k}\sigma}^+ b_{\mathbf{k}\sigma} + \lambda_{\mathbf{k}} p_{z\mathbf{k}\sigma}^+ a_{\mathbf{k}\sigma} + \text{h.c.}) \\ &= -2t_{pp}'\sum_{\mathbf{ij}\sigma}(\xi_{\mathbf{ij}\sigma} p_{z\mathbf{i}\sigma}^+ b_{\mathbf{j}\sigma} + \lambda_{\mathbf{ij}} p_{z\mathbf{i}\sigma}^+ a_{\mathbf{j}\sigma} + \text{h.c.}), \\ H_{pd}' &= -\frac{2t_{pd}'}{\sqrt{3}}\sum_{\mathbf{k}\sigma}(d_{z\mathbf{k}\sigma}^+ p_{z\mathbf{k}\sigma} + \text{h.c.}) \\ &= -\frac{2t_{pd}'}{\sqrt{3}}\sum_{\mathbf{ij}\sigma}(d_{z\mathbf{i}\sigma}^+ p_{z\mathbf{i}\sigma} + \text{h.c.}). \end{aligned} \tag{8}$$

As one can see from Eqs. (6) and (8), the dependences of the coefficients $\mu_{\mathbf{ij}}$, $\nu_{\mathbf{ij}}$, $\xi_{\mathbf{ij}}$, $\lambda_{\mathbf{ij}}$, and $\chi_{\mathbf{ij}}$ on the intersite distance $\Delta\mathbf{R}_{ij}$ completely determine in our approach the rules for and the magnitude of the hybridization of the oxygen molecular *a* and *b* orbitals with one another as well as with $d_{x^2-y^2}$ and d_{z^2} orbitals on different cells *i* and *j*. The functions are summarized in Table 1 [23]. In application to the Coulomb term, this procedure leads to three- and four-center contributions to the aggregate Hamiltonian:

$$\begin{aligned} H_{pd}^{\text{int}} &= \sum_{\mathbf{lij}}\sum_{\alpha\lambda\sigma\sigma'} V_{pd}\Phi_{\mathbf{lij}} n_{\lambda l}^{\sigma} p_{\alpha\mathbf{i}\sigma'}^+ p_{\alpha\mathbf{j}\sigma'}, \\ H_{pp}^{\text{int}} &= \sum_{\mathbf{ijkl}}\sum_{\alpha} U_p \Psi_{\mathbf{ijkl}} p_{\alpha\mathbf{i}\uparrow}^+ p_{\alpha\mathbf{j}\uparrow} p_{\alpha\mathbf{k}\downarrow}^+ p_{\alpha\mathbf{l}\downarrow}, \end{aligned} \tag{9}$$

where $p_{\alpha\mathbf{f}\sigma} = a_{\mathbf{f}\sigma}, b_{\mathbf{f}\sigma}$. Thus, aside from the standard single-center Coulomb interaction, we obtain additional contributions, for example, to the part of the aggregate Hamiltonian that takes account of hops $\sim V_{pd}\Phi_{\mathbf{ij}} n_{\lambda\mathbf{i}}^{\sigma} p_{\alpha\mathbf{i}\sigma'}^+ p_{\alpha\mathbf{j}\sigma'}$. Direct calculations of the coefficients $\Phi_{\mathbf{lij}}$ and $\Psi_{\mathbf{klij}}$ show that $\Phi_{000} = 0.918$, $\Phi_{001} = -0.13$, $\Phi_{002} = -0.02$, $\Psi_{0000} = 0.2109$, and $\Psi_{0001} = -0.03$. Since the computed coefficients depend strongly on the distance, we retain in what follows the strongest single-center interactions:

$$\begin{aligned} H_{pd}^{\text{int}} &= V_{pd}\Phi_{000}\sum_{\mathbf{i}\alpha\lambda\sigma\sigma'} n_{\lambda\mathbf{i}}^{\sigma} n_{\alpha\mathbf{i}}^{\sigma'}, \\ H_{pd}^{\text{int}} &= U_p \Psi_{0000}\sum_{\alpha\mathbf{i}} n_{\alpha\mathbf{i}}^{\uparrow} n_{\alpha\mathbf{i}}^{\downarrow}. \end{aligned} \tag{10}$$

Table 1. Dependence of the matrix elements on the distance (*ij*) [23]

	00	10	11	20	21	22
μ	0.95809	−0.14009	−0.02351	−0.01373	−0.00685	−0.00327
ν	0.72676	−0.27324	0.12207	−0.06385	0.01737	0.01052
λ	0.74587	−0.17578	0.06179	−0.07134	0.01703	0.00925
ξ	0.00000	0.25763	0.00000	0.03913	0.00886	0.00000
χ	0.00000	0.13397	0.00000	−0.04056	0.03043	0.00000

Thus, after this step our Hamiltonian becomes a sum of intracell and intercell terms:

$$H = H_c + H_{cc}, \quad H_c = \sum_{\mathbf{f}\sigma} H_{\mathbf{f}\sigma}, \tag{11}$$

$$H_{\mathbf{f}\sigma} = h^{(a)} + h^{(b)} + h^{(ab)},$$

$$h^{(a)} = (\varepsilon_a n_a^\sigma + \varepsilon_{d_z} n_{d_z}^\sigma + \varepsilon_{p_z} n_{p_z}^\sigma) + \frac{1}{2} U_d n_{d_z}^\sigma n_{d_z}^{-\sigma} + \frac{1}{2} U_a n_a^\sigma n_a^{-\sigma} + \frac{1}{2} U'_p n_{p_z}^\sigma n_{p_z}^{-\sigma} + \sum_{\sigma'} (V'_{pd} n_{d_z}^\sigma n_{p_z}^{\sigma'} + V_{pd} n_{d_z}^\sigma n_a^{\sigma'}) + \tau_a (d_{z\sigma}^+ a_\sigma + \text{h.c.}) - \tau'_{pd} (d_{z\sigma}^+ p_{z\sigma} + \text{h.c.}) - t'_{pp} (a_\sigma^+ p_{z\sigma} + \text{h.c.}),$$

$$h^{(b)} = (\varepsilon_b n_b^\sigma + \varepsilon_{d_x} n_{d_x}^\sigma) + \frac{1}{2} U_d n_{d_x}^\sigma n_{d_x}^{-\sigma} + \frac{1}{2} U_b n_b^\sigma n_b^{-\sigma} + \sum_{\sigma'} V_{pd} n_{d_x}^\sigma n_b^{\sigma'} - \tau_b \sum_\sigma (d_{x\sigma}^+ b_\sigma + \text{h.c.}),$$

$$h^{(ab)} = \sum_{\sigma'} U_d n_{d_x}^\sigma n_{d_x}^{\sigma'} + U_{ab} n_a^\sigma n_b^{\sigma'} + V_{pd} n_{d_x}^\sigma n_a^{\sigma'} + V_{pd} n_b^\sigma n_{d_x}^{\sigma'} + V'_{pd} n_{d_x}^\sigma n_{p_x}^{\sigma'},$$

$$H_{cc} = \sum_{(\mathbf{i} \neq \mathbf{j})} \sum_\sigma (h_{\text{hop}}^{(a)} + h_{\text{hop}}^{(b)} + h_{\text{hop}}^{(ab)}),$$

$$h_{\text{hop}}^{(a)} = \frac{2t_{pd}}{\sqrt{3}} \lambda_{\mathbf{ij}} (d_{\mathbf{i}z\sigma}^+ a_{\mathbf{j}\sigma} + \text{h.c.}) + 2t_{pp} \nu_{\mathbf{ij}} a_{\mathbf{i}\sigma}^+ a_{\mathbf{j}\sigma} - 2t'_{pp} \lambda_{\mathbf{ij}} (p_{\mathbf{i}z\sigma}^+ a_{\mathbf{j}\sigma} + \text{h.c.}),$$

$$h_{\text{hop}}^{(b)} = -2t_{pd} \mu_{\mathbf{ij}} (d_{\mathbf{i}x\sigma}^+ b_{\mathbf{j}\sigma} + b_{\mathbf{i}\sigma}^+ d_{\mathbf{i}x\sigma}) - 2t_{pp} \nu_{\mathbf{ij}} b_{\mathbf{i}\sigma}^+ b_{\mathbf{j}\sigma},$$

$$h_{\text{hop}}^{(ab)} = \frac{2t_{pd}}{\sqrt{3}} \xi_{\mathbf{ij}} (d_{\mathbf{i}z\sigma}^+ b_{\mathbf{j}\sigma} + \text{h.c.}) + 2t_{pp} \chi_{\mathbf{ij}} (a_{\mathbf{i}\sigma}^+ b_{\mathbf{j}\sigma} + \text{h.c.}) - 2t'_{pp} \xi_{\mathbf{ij}} (p_{\mathbf{i}z\sigma}^+ b_{\mathbf{j}\sigma} + \text{h.c.}),$$

where

$$\varepsilon_b = \varepsilon_p - 2t_{pp}\nu_{00}, \quad \varepsilon_a = \varepsilon_p + 2t_{pp}\nu_{00},$$

$$\tau_b = 2t_{pd}\mu_{00}, \quad \tau_a = \frac{2t_{pd}\lambda_{00}}{\sqrt{3}},$$

$$\tau'_{pd} = \frac{2t'_{pd}}{\sqrt{3}}, \quad \tau'_{pp} = 2t'_{pp}\lambda_{00}.$$

In what follows, as a simplification, we shall drop the coefficients Ψ_{000} and Φ_{000} when we write the Coulomb interaction parameters: $U_a = U_{ab} = U'_p = U_b = U_p\Psi_{000}$, $V_{pd} = V_{pd}\Psi_{000}$. Besides these parameters, which refer to the Coulomb interaction in a plane, there are also parameters characterizing the analogous interaction with the apical oxygen V'_{pd}. The coefficients μ_{ij}, ν_{ij}, and λ_{ij} refer to hybridization of states possessing the same symmetry and depend only on the distance between the i and j sites. The coefficients ξ_{ij} and χ_{ij} refer to the hybridization of the states belonging to different a_1 and b_1 representations, and they change sign on reflection along one of the x or y axes. The Hamiltonian (11) does not contain hops $d_z \longleftrightarrow d_z$, $p_z \longleftrightarrow p_z$, and $d_z \longleftrightarrow p_z$. The holes in these states are less "mobile" than in the planar d_x, b, and a states.

As the next step, we shall determine the eigenvalues and eigenstates of the single-cell Hamiltonian H_c that can be found exactly and we shall then rewrite the total Hamiltonian H in terms of these eigenstates. In the vacuum sector we have the proper state $d^{10}p^6$ or $|0\rangle$. In the single-hole b_1 sector in the basis of $|d_{x\sigma}^+|0\rangle$ and $|b_\sigma^+|0\rangle$ states the eigenvectors $|\tilde{b}_p\rangle = \beta_p(b)|b_\sigma^+|0\rangle + \beta_p(d_x)|d_{x\sigma}^+|0\rangle$ with energies $\varepsilon_{1\tilde{b}_p}$, $p = 1, 2$, can be found by exact diagonalization

$$\hat{h}^{(b)} = \begin{pmatrix} \varepsilon_{d_x} & -\tau_b \\ -\tau_b & \varepsilon_b \end{pmatrix}. \tag{12}$$

In the single-hole a_1 sector in the basis $|a_\sigma^+|0\rangle$, $|p_{z\sigma}^+|0\rangle$, and $|d_{z\sigma}^+|0\rangle$ states, the eigenvectors $|\tilde{a}_p\rangle = \alpha_p(a)|a_\sigma^+|0\rangle + \alpha_p(p_z)|p_\sigma^+|0\rangle + \alpha_p(d_z)|d_{z\sigma}^+|0\rangle$ with energies $\varepsilon_{1\tilde{a}_p}$, $p = 1, 2, 3$ can be found by exact diagonalization

$$\hat{h}^{(a)} = \begin{pmatrix} \varepsilon_{d_z} & \tau_a & -\tau'_{pd} \\ \tau_a & \varepsilon_a & -t'_{pp} \\ -\tau'_{pd} & -t'_{pp} & \varepsilon_{p_z} \end{pmatrix}. \tag{13}$$

The eigenstates of a cell in the two-hole A_1 sector $|\tilde{A}_q\rangle = \sum_i A_{qi}|A_i\rangle$, where the coefficients are the eigenvectors A_{qi} (i, q = 1–9), and the set of basis singlet functions $|A_i\rangle$ are presented in Table 2. The $|\tilde{A}_q\rangle$ eigenstates with energy $\varepsilon_{2\tilde{A}_q}$ can be found by exact diagonalization of the matrix

$$\hat{h}^{(A)} = \begin{pmatrix} \hat{h}_{11}^{(A)} & 0 \\ 0 & \hat{h}_{22}^{(A)} \end{pmatrix}, \tag{14}$$

$$\text{where } \hat{h}_{11}^{(A)} = \begin{pmatrix} \varepsilon_b + \varepsilon_{d_x} + V_{pd} & -\sqrt{2}\tau_b & \sqrt{2}\tau_b \\ -\sqrt{2}\tau_b & 2\varepsilon_b + U_b & 0 \\ -\sqrt{2}\tau_b & 0 & 2\varepsilon_{d_x} + U_d \end{pmatrix},$$

$$\hat{h}_{22}^{(A)} = \begin{pmatrix} \varepsilon_a + \varepsilon_{p_z} + V'_p & -\tau'_{pd} & \tau_a & -\sqrt{2}t'_{pp} & -\sqrt{2}t'_{pp} & 0 \\ -\tau'_{pd} & \varepsilon_{d_z} + \varepsilon_a + V_{pd} & -t'_{pp} & \sqrt{2}\tau_a & 0 & \sqrt{2}\tau_a \\ \tau_a & -t'_{pp} & \varepsilon_{d_z} + \varepsilon_{p_z} + V'_{pd} & 0 & -\sqrt{2}\tau'_{pd} & -\sqrt{2}\tau'_{pd} \\ -\sqrt{2}t'_{pp} & \sqrt{2}\tau_a & 0 & 2\varepsilon_a + U_a & 0 & 0 \\ -\sqrt{2}t'_{pp} & 0 & -\sqrt{2}\tau'_{pd} & 0 & 2\varepsilon_{p_z} + U'_p & 0 \\ 0 & \sqrt{2}\tau_a & -\sqrt{2}\tau'_{pd} & 0 & 0 & 2\varepsilon_{d_z} + U_d \end{pmatrix}. \tag{15}$$

In addition, the Zhang–Rice singlet $|ZR\rangle$ appears in it as one of the basis states. In the two-hole sector B_1 we seek the triplet eigenvectors in the form $|\tilde{B}_{qM}\rangle = \sum_i B_{qi}|B_{iM}\rangle$ (q = 1–6, M = –1, 0, 1), where the corresponding coefficients B_{qi} and the set of basis functions $|B_{qM}\rangle$ are presented in Table 3 with energies $\varepsilon_{2\tilde{B}_q}$ found by diagonalizing the matrix

$$\hat{h}^{(\tilde{B})} = \begin{pmatrix} \varepsilon_a + \varepsilon_{d_x} + V_{pd} & -\tau_b & \tau_a & 0 & -t'_{pp} & 0 \\ -\tau_b & \varepsilon_a + \varepsilon_b + V_b & 0 & \tau_a & 0 & -t'_{pp} \\ \tau_a & 0 & \varepsilon_{d_z} + \varepsilon_{d_x} + V_d & -\tau_b & -\tau'_{pd} & 0 \\ 0 & \tau_a & -\tau_b & \varepsilon_{d_z} + \varepsilon_b + V_{pd} & 0 & -\tau'_{pd} \\ -t'_{pp} & 0 & -\tau'_{pd} & 0 & \varepsilon_{d_x} + \varepsilon_{p_z} + V'_{pd} & -\tau_b \\ 0 & -t'_{pp} & 0 & -\tau'_{pd} & -\tau_b & \varepsilon_b + \varepsilon_{p_z} + V'_{pp} \end{pmatrix}. \tag{16}$$

Diagonalization of the Hamiltonian for a CuO_6 cluster is done separately in different sectors with n = 0, 1, and 2 holes. The vacuum section n = 0 corresponds to the $3d^{10}$ configuration of copper and the $2p^6$ configuration of oxygen. Figure 2 shows the energies of the competing singlet $|\tilde{A}_p\rangle$ (p = 1, 2) and triplet $|\tilde{B}_{1M}\rangle$ states as a function of the crystal field parameter $\Delta_d = \varepsilon_{d_z} - \varepsilon_{d_x}$, the difference in the energies of the $2p$ orbitals of the planar and apical oxygen $\Delta_{ap} = \varepsilon_p - \varepsilon_{p_z}$, and the ratio d_{ap}/d_{pl} of the distances from the copper atom to the apical and the planar oxygen atoms. The energy of the state $|\tilde{A}_1\rangle = A_1(d_xb)|ZR\rangle + A_3(d_xd_x)|A_3\rangle + A_2(bb)|A_2\rangle$ does not depend on the values of the parameters presented above. The contributions from the cell orbitals in

Table 2. Eigenvectors A_{qi} and the set of basis singlet functions $|A_i\rangle$

i	A_{qi}	$\lvert A_i\rangle$
1	$A_q(d_xb)$	$\lvert ZR\rangle = \frac{1}{\sqrt{2}}\lvert d^+_{x\downarrow}b^+_\uparrow - d^+_{x\uparrow}b^+_\downarrow\rvert 0\rangle$
2	$A_q(bb)$	$\lvert b^+_\downarrow b^+_\uparrow\rvert 0\rangle$
3	$A_q(d_xd_x)$	$\lvert d^+_{x\downarrow}d^+_{x\uparrow}\rvert 0\rangle$
4	$A_q(p_za)$	$\frac{1}{\sqrt{2}}\lvert p^+_{z\downarrow}a^+_\uparrow - p^+_{z\uparrow}a^+_\downarrow\rvert 0\rangle$
5	$A_q(d_za)$	$\frac{1}{\sqrt{2}}\lvert d^+_{z\downarrow}a^+_\uparrow - d^+_{z\uparrow}a^+_\downarrow\rvert 0\rangle$
6	$A_q(d_zp_z)$	$\frac{1}{\sqrt{2}}\lvert d^+_{z\downarrow}p^+_{z\uparrow} - d^+_{z\uparrow}p^+_{z\downarrow}\rvert 0\rangle$
7	$A_q(aa)$	$\lvert a^+_\downarrow a^+_\uparrow\rvert 0\rangle$
8	$A_q(p_zp_z)$	$\lvert p^+_{z\downarrow}p^+_{z\uparrow}\rvert 0\rangle$
9	$A_q(d_zd_z)$	$\lvert d^+_{z\downarrow}d^+_{z\uparrow}\rvert 0\rangle$

the other two states $|\tilde{A}_2\rangle$ and $|\tilde{B}_{1M}\rangle$ change strongly together with the values of the parameters, and they cannot be identified with any specific orbitals from the molecular orbitals with the same symmetry.

As the energy of the 2*p* orbital of apical oxygen decreases, the state $|\tilde{B}_{1M}\rangle$ is observed to approach the singlet $|\tilde{A}_1\rangle$ (Fig. 2b). Together with the tendency for crossover, there is also an appreciable increase in the fraction of the d_xp_z-symmetrized configuration in $|\tilde{B}_{1M}\rangle$. It is important to note that this is only the first main mechanism of stabilization of the $|\tilde{B}_{1M}\rangle$ state, and it is related with the large contribution from the d_xp_z-symmetrized configuration. The increase of this contribution is confirmed by this dependence as well as the dependence shown in Fig. 2a. Therefore, the same stabilization mechanism operates in both cases. However, in the first case its nature is associated with the decrease in the energy of the p_z orbital, whereas in the second case it is associated with the dependence of the corresponding hopping integral on the distance to the apical oxygen. A decrease in the energies of the p_z orbitals gives rise more effectively to an increase in the d_xp_z contribution in the ground two-hole state.

A decrease of the parameter $\Delta_d = \varepsilon_{d_z} - \varepsilon_{d_z}$ (Fig. 3c) results in an increase in the Hund state fraction and ultimately convergence of the ground $|\tilde{A}_1\rangle$ singlet and the $|\tilde{B}_{1M}\rangle$ states. This is the second basic mechanism for stabilization of the $|\tilde{B}_{1M}\rangle$ state. Since it is associated with a gain in the Hund interaction with an increasing contribution of the d_xd_z configuration, it is all the more effective the higher the energy of the 2*p* orbital of the planar oxygen and the lower the energy of the d_z orbital. For this method of stabilization of the $|\tilde{B}_{1M}\rangle$ state, the fraction of p_z states decreases in this state, and the fraction of the Hund configuration d_xd_z, through which the population of the d_z orbitals could be observed, increases.

Table 3. Eigenvectors B_{qi} and the set of basis functions $|B_{iM}\rangle$

i	B_{qi}	$\lvert B_{i-1}\rangle$	$\lvert B_{i0}\rangle$	$\lvert B_{i1}\rangle$
1	$B_q(d_xa)$	$\lvert d^+_{x\downarrow}a^+_\downarrow\rvert 0\rangle$	$\frac{1}{\sqrt{2}}\lvert d^+_{x\downarrow}a^+_\uparrow + d^+_{x\uparrow}a^+_\downarrow\rvert 0\rangle$	$\lvert d^+_{x\uparrow}a^+_\uparrow\rvert 0\rangle$
2	$B_q(ba)$	$\lvert b^+_\downarrow a^+_\downarrow\rvert 0\rangle$	$\frac{1}{\sqrt{2}}\lvert b^+_\downarrow a^+_\uparrow + b^+_\uparrow a^+_\downarrow\rvert 0\rangle$	$\lvert b^+_\uparrow a^+_\uparrow\rvert 0\rangle$
3	$B_q(d_xd_z)$	$\lvert d^+_{x\downarrow}d^+_{z\downarrow}\rvert 0\rangle$	$\frac{1}{\sqrt{2}}\lvert d^+_{x\downarrow}d^+_{z\uparrow} + d^+_{x\downarrow}d^+_{z\uparrow}\rvert 0\rangle$	$\lvert d^+_{x\uparrow}d^+_{z\uparrow}\rvert 0\rangle$
4	$B_q(d_xb)$	$\lvert d^+_{x\downarrow}b^+_\downarrow\rvert 0\rangle$	$\frac{1}{\sqrt{2}}\lvert d^+_{x\downarrow}b^+_\uparrow + d^+_{x\uparrow}b^+_\downarrow\rvert 0\rangle$	$\lvert d^+_{z\uparrow}b^+_\uparrow\rvert 0\rangle$
5	$B_q(d_xp_z)$	$\lvert d^+_{x\downarrow}p^+_{z\downarrow}\rvert 0\rangle$	$\frac{1}{\sqrt{2}}\lvert d^+_{x\downarrow}p^+_{z\uparrow} + d^+_{x\downarrow}p^+_{z\uparrow}\rvert 0\rangle$	$\lvert d^+_{x\uparrow}p^+_{z\uparrow}\rvert 0\rangle$
6	$B_q(bp_z)$	$\lvert b^+_\downarrow p^+_{z\downarrow}\rvert 0\rangle$	$\frac{1}{\sqrt{2}}\lvert b^+_\downarrow p^+_{z\uparrow} + b^+_\uparrow p^+_{z\downarrow}\rvert 0\rangle$	$\lvert b^+_\uparrow p^+_{z\uparrow}\rvert 0\rangle$

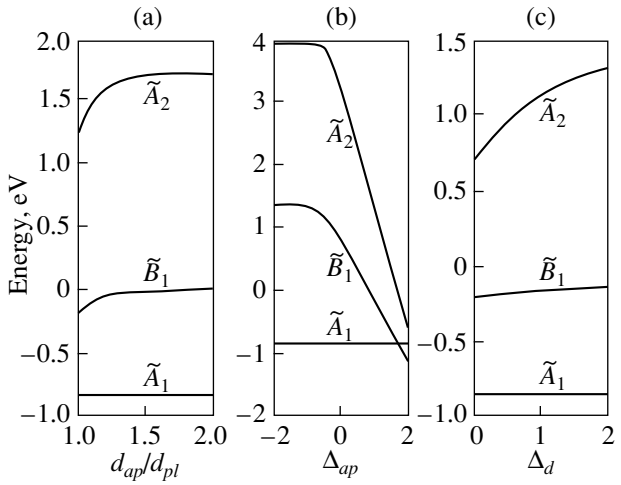

Fig. 2. Energies of $|\tilde{A}_1\rangle$, $|\tilde{A}_2\rangle$, and $|\tilde{B}_{1M}\rangle$ two-hole states versus the ratio d_{ap}/d_{pl} of the distances from the copper atom to the apical oxygen to the analogous distance to the planar oxygen, where $\Delta_d = 2$ eV and $\Delta_{ap} = 0.5$ eV (a) and versus the energy difference between the $2p$ orbitals of the planar and apical oxygen: $\Delta_{ap} = \varepsilon_p - \varepsilon_{p_z}$, where $d_{ap}/d_{pl} = 1.2$, $\Delta_d = 2$ eV (b), and versus the crystal field parameter $\Delta_d = \varepsilon_{d_z} - \varepsilon_{d_x}$, where $d_{ap}/d_{pl} = 1.2$, $\Delta_d = 0.5$ eV (c).

Thus, the energy splitting between the triplet and singlet states is $\Delta\varepsilon_2 \approx 0.5$ eV (Fig. 3a). Consequently, the presence of two states $|\tilde{A}_1\rangle$ and $|\tilde{B}_{1M}\rangle$, competing in energy, for realistic values of the parameters makes it necessary to take them into account simultaneously as basis states in our model and makes it impossible further reduction to an effective one-band Hubbard model. As a result of exact diagonalization, the Hamiltonian H_c for the antiferromagnetic phase becomes

$$H_c = \sum_{p\mathbf{f}_G\sigma} (\varepsilon_{1pG} - \mu) X^{pp}_{\mathbf{f}_G\sigma} + \sum_{q\mathbf{f}_G\sigma} (\varepsilon_{2qG} - 2\mu) X^{qq}_{\mathbf{f}_G\sigma}, \quad \text{where } f_G = \begin{cases} \mathbf{f}_A, & \mathbf{f} \in A \\ \mathbf{f}_B, & \mathbf{f} \in B. \end{cases} \tag{17}$$

Here p and q *e*numerate the single- and two-hole terms of a cell; $X^{pq}_{\mathbf{f}} = |p\rangle\langle q|$ are Hubbard operators constructed on the exact states of a cell. The sublattice levels are split by the field of the antiferromagnetic state: $\varepsilon_{1pA} = \varepsilon_{1p} - \sigma h$ and $\varepsilon_{1pB} = \varepsilon_{1p} + \sigma h$. The quantity $h \sim J\langle S_z\rangle$, where the effective exchange interaction of nearest neighbors $J \sim t'^2_{\text{eff}}/(\varepsilon_{20} - 2\varepsilon_{10})$ and t'_{eff} is determined below (see Eq. (29)); ε_{10} and ε_{20} are the energies of the bottom single- and two-particle terms. Doping decreases h, which vanishes in the paramagnetic phase. In the present work we confine our attention to a nonself-consistent calculation, in which the magnetic state is assumed to be given (antiferromagnetic or paramagnetic). On the other hand the role of the field h is to separate the sublattices, just as in Bogolyubov's method of quasiaverages. Effects due to the change in h taking account of doping give band shifts by an amount of the order of 10^{-3} eV, which is less than the resolution of modern photoelectronic methods; we shall neglect these effects. In the new basis the single-electron operators become

$$c_{\mathbf{f}\lambda\sigma} = \sum_m \gamma_{\lambda\sigma}(m) X^m_{\mathbf{f}\sigma}, \tag{18}$$

where $c_{\lambda\mathbf{f}\sigma} = d_{x\mathbf{f}\sigma}, d_{z\mathbf{f}\sigma}, a_{\mathbf{f}\sigma}, b_{\mathbf{f}\sigma}, p_{z\mathbf{f}\sigma}$ and m is the number of the root vector $\boldsymbol{\alpha}_m(pq)$. Here, to make it easier to work with Hubbard operators, we employ the notation of Zaitsev [30], where to each pair (initial–final) of states $|q\rangle \longrightarrow |p\rangle$ there is associated a root vector $\boldsymbol{\alpha}_m(pq)$, so that

$$X^{pq}_{\mathbf{f}\sigma} \longrightarrow X^{\boldsymbol{\alpha}_m(pq)}_{\mathbf{f}\sigma} \longrightarrow X^m_{\mathbf{f}\sigma}.$$

The matrix elements of the hopping amplitudes $\gamma_{\lambda\sigma}(m)$ ($m = 1, 2, \ldots, 32$), corresponding to these root vectors, can be calculated directly by performing an exact diagonalization of the Hamiltonian H_c and are presented in Tables 4–6. Only the two bottom terms (b_1 and a_1) are taken into account in the single-particle sector and $\tilde{A}_1$, $\tilde{B}_{1M}$ are taken into account in the two-particle sector. Therefore in Eq. (17) $|p\rangle = |\tilde{a}_1\rangle$, $|\tilde{b}_1\rangle$ and $|q\rangle = \tilde{A}_1$, $\tilde{B}_{1M}$. All other terms correspond to a higher energy and are of no significance for the physics of low-energy excitations.

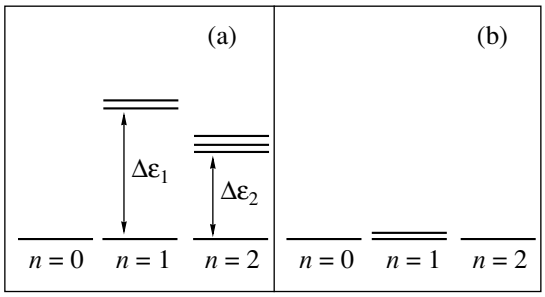

Fig. 3. Sets of basal states for realistic multiband *pd* model (a) and for a single-band Hubbard model (b).

Table 4. Matrix elements for quasiparticle excitations $\alpha_m(\tilde{b}_{1\sigma'}\tilde{A}_1)$. Here c_i denotes d_x or b

$\mathbf{f}_G$	$\mathbf{f}_A$		$\mathbf{f}_B$	
σ'	$\uparrow$	$\downarrow$	$\uparrow$	$\downarrow$
m	1	9	17	25
$\gamma_{d_x\sigma}$	$\eta(\sigma)(\delta_{\sigma\sigma'} - 1)\sum_i \beta_1(c_i) A_1(d_x c_i)$			
$\gamma_{b\sigma}$	$\eta(\sigma)(\delta_{\sigma\sigma'} - 1)\sum_i \beta_1(c_i) A_1(b c_i)$			

Let $\mathbf{R}_1$ in the two-sublattice case refer to the intrasublattice neighbors and $\mathbf{R}_2$ to the intersublattice neighbors. Then the Hamiltonian of intercell hops can be written in the matrix form

$$H_{cc} = \begin{pmatrix} H_{AA} & H_{AB} \\ H_{BA} & H_{BB} \end{pmatrix} = \sum_{\lambda\lambda'\sigma} \begin{pmatrix} \sum_{\mathbf{fR}_1} T_{\lambda\lambda'}(\mathbf{R}_1)(c^+_{\mathbf{f}\lambda\sigma} c_{\mathbf{f}+\mathbf{R}_1\lambda'\sigma} + \text{h.c.}) & \sum_{\mathbf{fR}_2} T_{\lambda\lambda'}(\mathbf{R}_2)(c^+_{\mathbf{f}\lambda\sigma} c_{\mathbf{f}+\mathbf{R}_2\lambda'\sigma} + \text{h.c.}) \\ \sum_{\mathbf{gR}_2} T_{\lambda\lambda'}(\mathbf{R}_2)(c^+_{\mathbf{g}\lambda\sigma} c_{\mathbf{g}+\mathbf{R}_2\lambda'\sigma} + \text{h.c.}) & \sum_{\mathbf{gR}_1} T_{\lambda\lambda'}(\mathbf{R}_1)(c^+_{\mathbf{g}\lambda\sigma} c_{\mathbf{g}+\mathbf{R}_1\lambda'\sigma} + \text{h.c.}) \end{pmatrix} \tag{19}$$

$$= \sum_{\lambda\lambda'\sigma kmn} \gamma^*_{\lambda\sigma}(m)\gamma_{\lambda'\sigma}(n) \begin{pmatrix} T^{AA}_{\lambda\lambda'}(\mathbf{k}) X^{+m}_{\mathbf{k}\sigma} X^n_{\mathbf{k}\sigma} & T^{AB}_{\lambda\lambda'}(\mathbf{k}) X^{+m}_{\mathbf{k}\sigma} Y^n_{\mathbf{k}\sigma} \\ T^{BA}_{\lambda\lambda'}(\mathbf{k}) X^{+m}_{\mathbf{k}\sigma} Y^n_{\mathbf{k}\sigma} & T^{BB}_{\lambda\lambda'}(\mathbf{k}) Y^{+m}_{\mathbf{k}\sigma} Y^n_{\mathbf{k}\sigma} \end{pmatrix} + \text{h.c.},$$

where

$$T^{AA}_{\lambda\lambda'}(\mathbf{k}) = T^{BB}_{\lambda\lambda'}(\mathbf{k}) = \frac{2}{N}\sum_{\mathbf{R}_1} T^{AA}_{\lambda\lambda'}(\mathbf{R}_1) e^{i\mathbf{k}\cdot\mathbf{R}_1},$$

$$T^{AB}_{\lambda\lambda'}(\mathbf{k}) = T^{BA}_{\lambda\lambda'}(\mathbf{k}) = \frac{2}{N}\sum_{\mathbf{R}_2} T^{AB}_{\lambda\lambda'}(\mathbf{R}_2) e^{i\mathbf{k}\cdot\mathbf{R}_2},$$

$X^m_{\mathbf{k}\sigma}$ and $Y^n_{\mathbf{k}\sigma}$ are the Fourier transforms of the Hubbard operators, respectively, with respect to the A and B sublattices. In the basis d_x, d_z, b, a, and p_z the matrix for intercell hops has the form

$$T_{\lambda\lambda'}(\mathbf{R}) = \begin{pmatrix} 0 & 0 & -2t_{pd}\mu_{\mathbf{ij}} & 0 & 0 \\ 0 & 0 & \frac{2t_{pd}}{\sqrt{3}}\xi_{\mathbf{ij}} & \frac{2t_{pd}}{\sqrt{3}}\lambda_{\mathbf{ij}} & 0 \\ -2t_{pd}\mu_{\mathbf{ij}} & \frac{2t_{pd}}{\sqrt{3}}\xi_{\mathbf{ij}} & -2t_{pp}\nu_{\mathbf{ij}} & 2t_{pp}\chi_{\mathbf{ij}} & -2t'_{pp}\xi_{\mathbf{ij}} \\ 0 & \frac{2t_{pd}}{\sqrt{3}}\lambda_{\mathbf{ij}} & 2t_{pp}\chi_{\mathbf{ij}} & 2t_{pp}\nu_{\mathbf{ij}} & -2t'_{pp}\lambda_{\mathbf{ij}} \\ 0 & 0 & -2t'_{pp}\xi_{\mathbf{ij}} & -2t'_{pp}\lambda_{\mathbf{ij}} & 0 \end{pmatrix}. \tag{20}$$

Table 5. Matrix elements for quasiparticle excitations $\alpha_m(\tilde{a}_{1\sigma'}\tilde{B}_{1M})$. Here c_i denotes d_z, a, p_z

α_m	$\alpha_m(\tilde{a}_{1\sigma'}\tilde{B}_{1-1})$				$\alpha_m(\tilde{a}_{1\sigma'}\tilde{B}_{10})$				$\alpha_m(\tilde{a}_{1\sigma'}\tilde{B}_{11})$			
$\mathbf{f}_G$	$\mathbf{f}_A$		$\mathbf{f}_B$		$\mathbf{f}_A$		$\mathbf{f}_B$		$\mathbf{f}_A$		$\mathbf{f}_B$	
σ'	↑	↓	↑	↓	↑	↓	↑	↓	↑	↓	↑	↓
m	2	10	18	26	3	11	19	27	4	12	20	27
$\gamma_{d_x\sigma}$	$\delta_{\sigma\sigma'}\sum_i \alpha_1(c_i)B_1(d_x c_i)$				$\frac{1}{\sqrt{2}}(1-\delta_{\sigma\sigma'})\sum_i \alpha_1(c_i)B_1(d_x c_i)$				$\delta_{\sigma\sigma'}\sum_i \alpha_1(c_i)B_1(d_x c_i)$			
$\gamma_{b\sigma}$	$\delta_{\sigma\sigma'}\sum_i \alpha_1(c_i)B_1(b c_i)$				$\frac{1}{\sqrt{2}}(1-\delta_{\sigma\sigma'})\sum_i \alpha_1(c_i)B_1(b c_i)$				$\delta_{\sigma\sigma'}\sum_i \alpha_1(c_i)B_1(b c_i)$			

Table 6. Matrix elements for the quasiparticle excitations $\alpha_m(\tilde{b}_{1\sigma'}\tilde{B}_{1M})$. Here c_i denotes d_x or b

α_m	$\alpha_m(\tilde{b}_{1\sigma'}\tilde{B}_{1-1})$				$\alpha_m(\tilde{b}_{1\sigma'}\tilde{B}_{10})$				$\alpha_m(\tilde{b}_{1\sigma'}\tilde{B}_{11})$			
$\mathbf{f}_G$	$\mathbf{f}_A$		$\mathbf{f}_B$		$\mathbf{f}_A$		$\mathbf{f}_B$		$\mathbf{f}_A$		$\mathbf{f}_B$	
σ'	↑	↓	↑	↓	↑	↓	↑	↓	↑	↓	↑	↓
m	5	13	21	28	6	14	22	29	7	15	23	21
$\gamma_{a\sigma}$	$-\delta_{\sigma\sigma'}\sum_i \beta_1(c_i)B_1(a c_i)$				$-\frac{1}{\sqrt{2}}(1-\delta_{\sigma\sigma'})\sum_i \beta_1(c_i)B_1(a c_i)$				$-\delta_{\sigma\sigma'}\sum_i \beta_1(c_i)B_1(a c_i)$			
$\gamma_{d_z\sigma}$	$-\delta_{\sigma\sigma'}\sum_i \beta_1(c_i)B_1(p_z c_i)$				$-\frac{1}{\sqrt{2}}(1-\delta_{\sigma\sigma'})\sum_i \beta_1(c_i)B_1(p_z c_i)$				$-\delta_{\sigma\sigma'}\sum_i \beta_1(c_i)B_1(p_z c_i)$			
$\gamma_{p_z\sigma}$	$-\delta_{\sigma\sigma'}\sum_i \beta_1(c_i)B_1(d_z c_i)$				$-\frac{1}{\sqrt{2}}(1-\delta_{\sigma\sigma'})\sum_i \beta_1(c_i)B_1(d_z c_i)$				$-\delta_{\sigma\sigma'}\sum_i \beta_1(c_i)B_1(d_z c_i)$			

3. DERIVATION OF THE DISPERSION RELATIONS

Next, we shall derive the corresponding dispersion relations for the valence band of a CuO_2 layer. For this, as already done in the generalized tight-binding method [15], we employ the Green's functions method. The equations of motion for the operators $X^m_{\mathbf{f}\sigma}$ and $Y^n_{\mathbf{g}\sigma}$ have the form

$$i\dot{X}^m_{\mathbf{f}\sigma} = [X^m_{\mathbf{f}\sigma}, H] = \Omega_m X^m_{\mathbf{f}\sigma} + [X^m_{\mathbf{f}\sigma}, H_{cc}], \qquad (21)$$

where $\Omega^G_m = \Omega_G(\boldsymbol{\alpha}_m) = \varepsilon_{2qG} - \varepsilon_{1pG}$. For any radius vector $\mathbf{R}$ the corresponding commutator can be calculated in the Hubbard 1 approximation:

$$[X^m_{\mathbf{f}\sigma}, H_{cc}]$$

$$= \sum_{\lambda\lambda'\sigma}\sum_{nl}\sum_{\mathbf{iR}} T_{\lambda\lambda'}(\mathbf{R})\{\gamma^*_{\lambda\sigma}(n)\gamma_{\lambda'\sigma}(l)[X^m_{\mathbf{f}\sigma}, X^{+n}_{\mathbf{i}\sigma'}X^l_{\mathbf{i}+\mathbf{R}\sigma'}] \qquad (22)$$

$$+ \gamma^*_{\lambda'\sigma'}(l)\gamma_{\lambda\sigma'}(n)[X^m_{\mathbf{f}\sigma}, X^{+l}_{\mathbf{i}+\mathbf{R}\sigma'}X^n_{\mathbf{i}\sigma}]\} \approx \sum_{\lambda\lambda' n\mathbf{R}} T_{\lambda\lambda'}(\mathbf{R})$$

$$\times \gamma^*_{\lambda\sigma}(n)\gamma_{\lambda'\sigma}(n)F_{\mathbf{f}\sigma}(m)(X^n_{\mathbf{f}+\mathbf{R}\sigma} + X^n_{\mathbf{f}-\mathbf{R}\sigma}),$$

where $F_{G\sigma}(m) = F_{G\sigma}(\boldsymbol{\alpha}_m(pq)) = \langle X^{pp}_{f_{G\sigma}}\rangle + \langle X^{qq}_{f_{G\sigma}}\rangle$ is the filling factor [30]. Hence, taking account of the existence of the *A* and *B* sublattices, we obtain the system of equations

$$i\dot{X}^m_{\mathbf{f}\sigma} = \Omega^A_m X^m_{\mathbf{f}\sigma} + 2\sum_{\lambda\lambda' n}\gamma^*_{\lambda\sigma}(m)\gamma_{\lambda'\sigma}(n)F_{A\sigma}(m)$$

$$\times\left(\sum_{\mathbf{R}_1} X^n_{\mathbf{f}+\mathbf{R}_1\sigma}T_{\lambda\lambda'}(\mathbf{R}_1) + \sum_{\mathbf{R}_2} Y^n_{\mathbf{f}+\mathbf{R}_2\sigma}T_{\lambda\lambda'}(\mathbf{R}_2)\right), \qquad (23)$$

$$i\dot{Y}^m_{\mathbf{g}\sigma} = \Omega^B_m X^m_{\mathbf{g}\sigma} + 2\sum_{\lambda\lambda' n\mathbf{R}}\gamma^*_{\lambda\sigma}(m)\gamma_{\lambda'\sigma}(n)F_{B\sigma}(m)$$

$$\times\left(\sum_{\mathbf{R}_1} Y^n_{\mathbf{g}+\mathbf{R}_1\sigma}T_{\lambda\lambda'}(\mathbf{R}_1) + \sum_{\mathbf{R}_2} X^n_{\mathbf{g}+\mathbf{R}_2\sigma}T_{\lambda\lambda'}(\mathbf{R}_2)\right).$$

For the matrix Green's function,

$$\hat{D}_{\mathbf{ij}} = \begin{pmatrix} \hat{D}_{\mathbf{ij}\sigma}(AA) & \hat{D}_{\mathbf{ij}\sigma}(AB) \\ \hat{D}_{\mathbf{ij}\sigma}(BA) & \hat{D}_{\mathbf{ij}\sigma}(BB) \end{pmatrix},$$

where $D^{mn}_{\mathbf{ij}\sigma}(AB) = \langle\langle X^n_{\mathbf{i}\sigma} | Y^n_{\mathbf{j}\sigma}\rangle\rangle$, we have an analogous system of equations:

$$D^{mn}_{\mathbf{ij}\sigma}(AA) = D^0_{m\sigma}(A)\delta_{\mathbf{ij}}\delta_{mn}$$

$$+ 2D^0_m(A)\sum_{\lambda\lambda' l}\gamma^*_{\lambda\sigma}(m)\gamma_{\lambda'\sigma}(l)$$

$$\times\left(\sum_{\mathbf{R}_1} T_{\lambda\lambda'}(\mathbf{R}_1)D^{ln}_{\mathbf{i}+\mathbf{R}_1\mathbf{j}\sigma}(AA)\right.$$

$$\left. + \sum_{\mathbf{R}_2} T_{\lambda\lambda'}(\mathbf{R}_2)D^{ln}_{\mathbf{i}+\mathbf{R}_2\mathbf{j}\sigma}(BA)\right), \qquad (24)$$

$$D^{mn}_{\mathbf{ij}\sigma}(BA) = 2D^0_{m\sigma}(B)\sum_{\lambda\lambda' l}\gamma^*_{\lambda\sigma}(m)\gamma_{\lambda'\sigma}(l)$$

$$\times\left(\sum_{\mathbf{R}_1} T_{\lambda\lambda'}(\mathbf{R}_1)D^{ln}_{\mathbf{i}+\mathbf{R}_1\mathbf{j}\sigma}(BA)\right.$$

$$\left. + \sum_{\mathbf{R}_2} T_{\lambda\lambda'}(\mathbf{R}_2)D^{ln}_{\mathbf{i}+\mathbf{R}_2\mathbf{j}\sigma}(AA)\right).$$

Here $D^0_{m\sigma}(A) = F_{A\sigma}(m)/(E - \Omega^A_m + i\varepsilon)$, i.e., the zero-approximation Green's function is diagonal with respect to the matrix indices *m* and *n*. After Fourier transforming

$$D^{mn}_{\mathbf{ij}} = \frac{2}{N}\sum_{\mathbf{k}} D^{mn}_{\mathbf{k}\sigma}e^{i\mathbf{k}\cdot(\mathbf{R}_i - \mathbf{R}_j)}$$

the system of equations becomes

$$D^{mn}_{\mathbf{k}\sigma}(AA) = D^0_m(A)\delta_{mn} + 2D^0_m(A)$$

$$\times\sum_{\lambda\lambda' l}\gamma^*_{\lambda\sigma}(m)\gamma_{\lambda'\sigma}(l)$$

$$\times[T^{AA}_{\lambda\lambda'}(\mathbf{k})D^{ln}_{\mathbf{k}\sigma}(AA) + T^{AB}_{\lambda\lambda'}(\mathbf{k})D^{ln}_{\mathbf{k}\sigma}(BA)], \qquad (25)$$

$$D^{mn}_{\mathbf{k}\sigma}(BA) = 2D^0_m(B)\sum_{\lambda\lambda' l}\gamma^*_{\lambda\sigma}(m)\gamma_{\lambda'\sigma}(l)$$

$$\times[T^{BB}_{\lambda\lambda'}(\mathbf{k})D^{ln}_{\mathbf{k}\sigma}(BA) + T^{BA}_{\lambda\lambda'}(\mathbf{k})D^{ln}_{\mathbf{k}\sigma}(AA)].$$

In the matrix form the system of equations (25) is

$$\hat{A}_\sigma(\mathbf{k})\hat{D}_{\mathbf{k}\sigma} = \hat{D}^0_\sigma,$$

$$\hat{A}_\sigma(\mathbf{k}) = \begin{pmatrix} 1 - \hat{D}^0_\sigma(A)\hat{T}^{AA}_{\text{eff}}(\mathbf{k},\sigma) & -\hat{D}^0_\sigma(A)\hat{T}^{AB}_{\text{eff}}(\mathbf{k},\sigma) \\ -\hat{D}^0_\sigma(B)\hat{T}^{BA}_{\text{eff}}(\mathbf{k},\sigma) & 1 - \hat{D}^0_\sigma(B)\hat{T}^{BB}_{\text{eff}}(\mathbf{k},\sigma) \end{pmatrix},$$

$$\hat{T}_{\text{eff}}(\mathbf{k},\sigma) = \begin{pmatrix} \hat{T}^{AA}_{\text{eff}}(\mathbf{k},\sigma) & \hat{T}^{AB}_{\text{eff}}(\mathbf{k},\sigma) \\ \hat{T}^{BA}_{\text{eff}}(\mathbf{k},\sigma) & \hat{T}^{BB}_{\text{eff}}(\mathbf{k},\sigma) \end{pmatrix}, \qquad (26)$$

$$T^{PG}_{\text{eff}mn}(\mathbf{k},\sigma) = \sum_{\lambda\lambda'}\gamma^*_{\lambda\sigma}(m)T^{PG}_{\lambda\lambda'}(\mathbf{k})\gamma_{\lambda'\sigma}(n).$$

Thus, the dispersion relations are determined by the equation for the poles of the matrix Green's function $\hat{D}$:

$$\left\| \frac{(E-\Omega_m^G)\delta_{mn}}{F_\sigma^G(m)} - 2\sum_{\lambda\lambda'}\gamma_{\lambda\sigma}^*(m)T_{\lambda\lambda}^{PG}(\mathbf{k})\gamma_{\lambda'\sigma}(n)\right\| = 0. \quad (27)$$

The equation (27) is similar to the standard single-electron equation for the tight-binding method, differing from it in two respects. In the first place, the single-particle energies are determined as resonances between multielectron states taking account of strong correlations. In the second place, the filling factors $F_\sigma^G(m)$ lead to a concentration dependence of the band structure of the quasiparticles. In the next section we shall present and discuss the results obtained by solving Eq. (27). The order of the determinant presented above is determined by the 32×32 matrix Green's function, constructed on a $m \times m$ basis from the root vectors. The equation (27) is an equation for the generalized eigenvalue problem, where a diagonal matrix of the inverse sum of the filling numbers of the initial and final states participating in the transition with a m root vector appear instead of the usual "nonorthogonality matrix." Each root vector $\boldsymbol{\alpha}_m$ determines a charged spin-1/2 Fermi quasiparticle; their local energies are Ω_m^G. The intercell hops lead to dispersion of the local quasiparticles.

4. COMPUTATIONAL RESULTS: DISPERSION RELATIONS AND ENERGY GAP IN AN UNDOPED DIELECTRIC WITH $x = 0$

Figure 4 shows the computational results for the undoped case (hole density $n_h = 1 + x = 1$) and the set of parameters in units of t_{pd}:

$$\varepsilon_{d_z} = 2, \quad \varepsilon_p = 1.6, \quad \varepsilon_{p_z} = 0.5,$$
$$t_{pp} = 0.46, \quad t'_{pp} = 0.42, \quad U_d = 9, \quad U_p = 4, \quad (28)$$
$$V_{pd} = 1.5, \quad J_d = 1.$$

The directions of the Brillouin zone for calculating the dispersion relations were chosen in accordance with the directions along which the ARPES observations were performed for antiferromagnetic dielectric compound $Sr_2CuO_2Cl_2$ [20]. The valence band top with prescribed values of the parameters is formed by quasiparticle states with root vectors $\boldsymbol{\alpha}_m(\tilde{b}_{1\sigma}\tilde{A}_1)$. In addition, the interband transitions with t_{pd}—the largest of the possible hopping integrals—are responsible for the dispersion of the wide valence band. The form of the valence band corresponds quantitatively to the ARPES-spectroscopy results for $Sr_2CuO_2Cl_2$ (Fig. 4). In this respect our calculation reproduces existing results for the dispersion of the valence band top on the basis of the t–t'–J model [19]. In contrast to the t–t'–J model, in our calculation there appears an additional zero-dispersion level at the valence band top, for which the filling factor and spectral weight ~x, i.e., they are zero in the undoped case. For $x = 0$ this level can be called virtual.

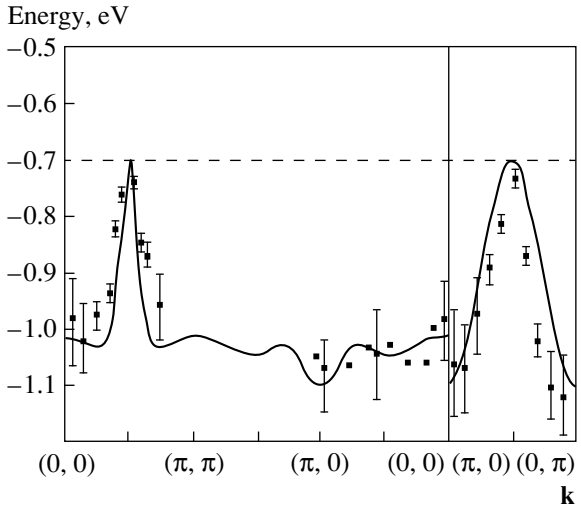

Fig. 4. Computed dispersion curves for $x = 0$ and directions of the Brillouin zone presented in the ARPES experiments (dots, $Sr_2CuO_2Cl_2$ [20]). The dashed line denotes the zero-dispersion virtual level with zero spectral density.

In the undoped antiferromagnetic case we are dealing with two quasiparticles at the valence band top: $\boldsymbol{\alpha}_m(\tilde{b}_{1\uparrow}\tilde{A}_1)$ and $\boldsymbol{\alpha}_m(\tilde{b}_{1\downarrow}\tilde{A}_1)$. At zero temperature, neglecting Coulomb fluctuations, the filling numbers of the $|\tilde{b}_{1\sigma}\rangle$ single-hole state for one spin projection are zero in the A and B sublattices. Consequently, for this spin projection a zero-dispersion level is present in the undoped case. Since transitions between empty states have zero amplitude, a peak corresponding to this transition is not observed in the spectral density, and only a peak corresponding to the valence band is detected. This is a typical effect of strong correlations. Similar effects have been observed previously for the density of states in the theory of magnetic semiconductors [31]. The valence band corresponds to a transition with the participation of a $|\tilde{b}_{1\sigma}\rangle$ state with nonzero filling numbers. A large effect of quasiparticles $\boldsymbol{\alpha}_m(\tilde{b}_{1\sigma}\tilde{B}_{1M})$ (with participation of a triplet) on the dispersion of the valence band is also observed. This is due to the small energy splitting, approximately 0.7 eV, between the triplet and ground singlet states in the two-hole sector of Hilbert space. The largest changes due to such a singlet-triplet hybridization are observed near the symmetry point $X = (\pi, 0)$. We reproduce the computational results obtained in the t–t'–J model [19] with $t'/t = -0.35$.

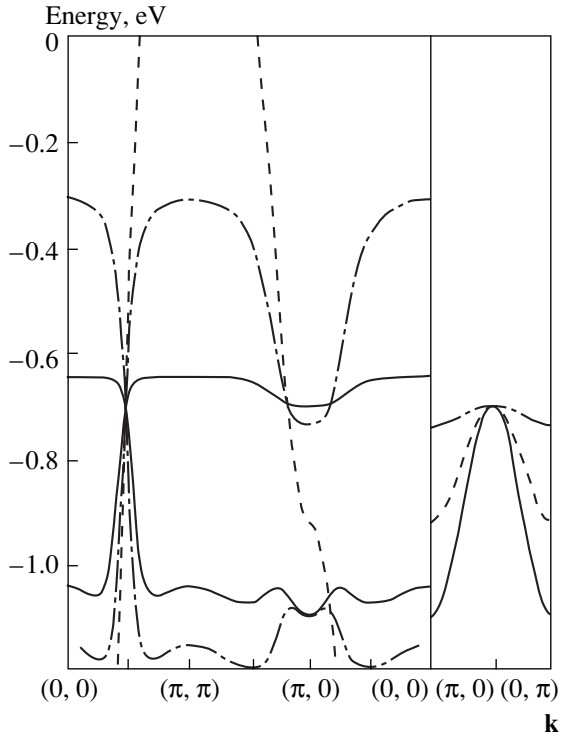

Fig. 5. Computed dispersion curves of the valence band of a CuO_2 layer in the antiferrophase: hole density $x = 0.01$ (solid line); hole density $x = 0.1$ (dot-dashed line); in the para phase the hole density $x = 0.2$ (dashed line).

In addition, in our case the ratio with a similar meaning

$$\frac{t'_{\text{eff}}}{t_{\text{eff}}} = \frac{t_{pd}\mu_{11}\varphi_d\varphi_p + t_{pp}\nu_{11}\varphi_p^2}{t_{pd}\mu_{10}\varphi_d\varphi_p + t_{pp}\nu_{10}\varphi_p^2} = -0.24, \qquad (29)$$

where

$$\varphi_d = \beta_1(d_x)A_1(d_xd_x) + \beta_1(b)A_1(d_xb),$$

$$\varphi_b = \beta_1(d_x)A_1(d_xb) + \beta_1(b)A_1(bb).$$

Contributions from intersublattice transitions to the dispersion of the valence band along the symmetric direction $X \longleftrightarrow Y$, i.e., along the boundary of the antiferromagnetic Brillouin zone, are forbidden. However, the width of the valence band in this direction and in $\Gamma = (0, 0) \longleftrightarrow M = (\pi, \pi)$, where intersublattice transitions contribute in the experiment [20], are approximately the same. In reality, because of the closeness of the triplet, the widths are determined not by the integral transfer, which is obviously much greater for intersublattice than for intrasublattice transitions, but rather by the hybridization of the singlet and lower-lying triplet valence bands. Neglecting the triplet, a much smaller dispersion was observed (just as in the *t–J* model [32]) in the direction $X \longleftrightarrow Y$ than in the direction $\Gamma \longleftrightarrow M$. The valence-band widths themselves, in this case, just as in the LDA calculations [33], were greater than the observed values.

The deeper valence bands are formed by quasiparticles $\boldsymbol{\alpha}_m(\tilde{a}_{1\sigma}\tilde{B}_{1M})$ and $\boldsymbol{\alpha}_m(\tilde{b}_{1\sigma}\tilde{B}_{1M})$. The former refer to transitions between empty excited states and have zero amplitude. In Fig. 4 these transitions correspond to a zero-dispersion level deep in the valence band. The second transitions form bands with much smaller dispersion than quasiparticles with $\boldsymbol{\alpha}_m(\tilde{b}_{1\sigma}\tilde{A}_1)$ root vectors, since they correspond only to hole transport with smaller hopping integrals t_{pd_z} or t_{pp}. This can be easily seen from the differences of Tables 4 and 6, where the amplitudes of the transitions $\gamma_{d_x\sigma}(m)$ and $\gamma_{b\sigma}(m)$ are zero for quasiparticles with vectors $\boldsymbol{\alpha}_m(\tilde{b}_{1\sigma'}\tilde{B}_{1M})$ and different from zero for $\boldsymbol{\alpha}_m(\tilde{b}_{1\sigma'}\tilde{A}_1)$ quasiparticles.

5. EFFECT OF DOPING ON THE BAND STRUCTURE OF THE QUASIPARTICLES OF A CuO_2 LAYER

The behavior of the zero-dispersions virtual level with doping is interesting. In the undoped case the filling numbers of both two-hole states $|\tilde{A}_1\rangle$ and $|B_{1M}\rangle$ are zero and correspond to a zero-dispersion virtual level. In the presence of doping the filling numbers of the two-hole state $|\tilde{A}_1\rangle$ are nonzero, $n_A = 1 + x$. In consequence, the initial virtual level acquires dispersion $\partial W/\partial x \sim 1$ eV. The wide valence band remains unchanged, since its filling factor $F = n_{\tilde{A}} + n_{\tilde{b}} = 1$ does not depend on the number of holes. Figure 5 shows the dispersion curves for $x = 0.01$ and for $x = 0.1$.

The largest changes with doping, as one can see by comparing Figs. 4 and 5, are due precisely to the dispersion of the previous virtual level; it is characterized by the wide maximum near the points Γ and M and minimum near the point X. At the same time the spectral density of the new valence band is proportional to the degree of doping x, i.e., this band is similar to the impurity bands in doped semiconductors. We underscore that in our approach there are no impurity effects in the form of fluctuations of the impurity potential or hopping integrals; doping influences only the hole density, and consequently the term "impurity" band signifies a band of quasiparticles whose spectral density for small $x \ll 1$ is proportional to the degree of doping. A mechanism, specific to strongly correlated systems, leading to the formation of impurity levels with doping has been discussed in detail on the basis of a two-orbital Hubbard model [27].

As the hole density increases with x changing from $x = 0.01$ to $x = 0.1$, the largest dispersion of the impurity band occurs near the points Γ and M with a further decrease of the minimum at the point X. However, a discussion of the high hole densities requires a special clarification. The point is that in principle the general approach formulated in Section 2 makes it possible to

study self-consistently the changes in the electronic and magnetic structures. However, our Hubbard 1 approximation for intercell hops leads to the fact that the magnetic system is described by an effective Heisenberg model, and its influence on the electronic system reduces to a redistribution of the filling numbers between the spin sublevels for a given sublattice. The applicability of such an approximation is analyzed in detail in [26], where it is shown that the results agree with the data obtained by exact diagonalization of small clusters by the Lanczos method for the Hubbard model and the *t–J* and three-band *p–d* models. Thus, comparing the perturbation theory for $J < t$ with the exact answers in the *t–J* model shows that the corrections to the vertices are small [34]. For the undoped case in the Hubbard model the spectral density of the quasiparticles, which is obtained by exact diagonalization, can be described in the mean-field theory (spin density waves) with a calculation of the magnetization of a sublattice in the spin-wave theory [35]. Consequently, we study the electronic structure against the background of a fixed magnetic order, which itself depends on the doping. Since on doping a *p*-type hole moves primarily along oxygen orbitals, additional exchange $J_{\text{Cu–O}} \gg J_{\text{Cu–Cu}}$ arises, resulting in frustrations in the Heisenberg antiferromagnet and rapid suppression of the three-dimensional antiferromagnetic long-range order. The critical densities [36, 37] and the concentration dependence of the Néel temperature $T_N(x)$ [38] were obtained in the *t–J* model in the spin-wave approach. Although there is no long-range antiferromagnetic order for $x > x_{cr}$, there does exist a two-dimensional short-range order with coherence length $x_{AFM} \gg a$ for lightly doped compositions, $x \ll 1$. Since the mean-free path length $l \sim a$ and $l \ll \xi_{AFM}$, the main effect of short-range order reduces to motion of an electron within an antiferromagnetic cluster, and the band structure can be interpreted similarly to a doped antiferromagnet even for $x > x_{cr}$ in the lightly doped range. The fluctuation character of a magnetic cluster introduces certain refinements in the picture described above. Specifically, instead of symmetry of bands with doubling of the Brillouin zone in an antiferromagnetic phase and the equivalence-coupled states k and $\mathbf{k} + \mathbf{Q}$ ($\mathbf{Q} = (\pi/a, \pi/a)$ is the nesting vector) which are equivalent because of Umpklapp processes, under conditions of short-range order the coupling of these states is of a dynamical character and is determined by the decay of the state $\mathbf{k}$, as a result of damping, into the final state $\mathbf{k} + \mathbf{Q}$ [39]. However, these differences are not fundamental, and a doped antiferromagnet with $x \sim 0.1$ will be studied in order to investigate the concentration evolution of the band structure. The transition from a doped antiferromagnet to an almost antiferromagnetic Fermi liquid seems to occur at $x \approx x_{\text{opt}}$, where $x_{\text{opt}} \approx 0.18$ is the optimal doping concentration for which $T_c(x)$ possesses a maximum. For optimal compositions $\xi_{AFM} \approx 2a$. Analysis of the concentration dependences of the two-magnon spectra of Bi-2212 led the authors of [40] likewise to the conclusion that crossover occurs between a doped antiferromagnet and an almost antiferromagnetic Fermi liquid at $x \approx x_{\text{opt}}$. In the paramagnetic phase the filling numbers of local terms do not depend on the spin index. Doubling of the Brillouin zone as compared with the antiferromagnetic phase removes the equivalence of the points Γ and M. Figure 5 shows (dashed lines) the band structure with $x = 0.2$ in the para phase. As one can see in Fig. 5, in the paramagnetic phase there is one valence band instead of two bands. The latter band reproduces well the dispersion curves calculated by the Monte Carlo method [19] and the dispersion curves observed for the optimally doped samples [41], including the Van Hove singularity near the symmetric point X.

6. DISCUSSION

The evolution of the band structure with doping can be traced by comparing Figs. 4 and 5. It is the dispersion of the impurity band and the merging of this band with the main band in the para phase that give the transition from an undoped structure with a maximum at the point $\overline{M} = (\pi/2, \pi/2)$ (Fig. 4) to the band structure of a doped system with a maximum at the point M and a saddlepoint X (Fig. 5). An important effect of magnetic order in the doped case is a gap between the impurity and the main valence bands at the point X. This gap is known as a pseudogap from NMR, inelastic neutron scattering, and ARPES experiments (see review [39]).

Spin fluctuations fall outside the scope of the present paper. Consequently, we cannot compare our results with the ARPES results and calculations of the spectral function on the basis of the quantum Monte Carlo method [19, 42] in the entire range of doped hole densities. However, for doping, an additional peak corresponding to a narrow impurity band and a high energy is added in our approach to the peak corresponding to a wide valence band and a quasiparticle state with wave vector $\mathbf{k}$. In addition, just as in [42], the behavior of the low-energy peak is identical to the behavior of the quasiparticle peak in the undoped case, since the dispersion of the wide valence band does not depend on the doping level. A high-energy peak is observed only in the doped variant, where the virtual level acquires dispersion. Indeed, as temperature decreases, for low degrees of doping, the Monte Carlo calculations for the *t–J* model [42] and calculations in the spin-bag model [43] show a similar splitting of the quasiparticle peak into two peaks—low and high energy. The splitting of the quasiparticle peaks in the spectral density occurs, according to [41] only near the symmetry point X. Calculations were performed for temperatures $T > 0.1t$. Lower temperatures are inaccessible because the influence of the finite size of the cluster in the analysis on the computational results cannot be controlled. This result becomes understandable if one keeps in mind the fact that, according to calcula-

tions in the theory of an almost antiferromagnetic liquid [44], hot regions, where quasiparticles are most sensitive to the short-range antiferromagnetic order, exist near the symmetry points X and Y on the Fermi surface. There is no splitting in the spectral function of the experimental ARPES investigations. Nonetheless, the presence of a pseudogap near X is indirect proof of the presence of a high-energy peak, lying above the Fermi level and consequently not observed in the ARPES experiment.

The mechanism for acquiring additional dispersion can be used to explain the ARPES-spectroscopy results concerning the opening of an energy gap along the line $X \longleftrightarrow M$ of the Brillouin zone [40] for $Bi_2Sr_2CaCu_2O_{8+\delta}$. Switching to dielectric samples, the form of the dispersion curves from Γ to $\overline{M}$ remains similar to the corresponding section of the dispersion curve of metallic samples. The dispersion curves near the point X behave completely differently. The transition from optimally doped metallic samples to lightly doped samples results in vanishing of the section of the Fermi surface on the line $X \longleftrightarrow M$. For samples with optimal doping (T_c = 85 K) large areas of the section of the Fermi surface were observed. If the rigid-band model were valid, then a decrease of hole density would result only in a decrease of the area of the section while its shape would remain unchanged. In addition, the intersections of the Fermi surface by the line $X \longleftrightarrow M$ should remain, which contradicts experiment, showing opening of an energy gap on the Fermi surface along the line $X \longleftrightarrow M$. In a dielectric sample the filling numbers of all two-hole states are zero, since transitions between empty states have zero amplitude, a peak corresponding to this transition is not observed in the spectral density (zero-dispersion virtual level), but rather a peak corresponding to the valence band for nonzero filling numbers of the state $|\tilde{b}_{1\sigma}\rangle$ for one of the spin projections is detected. For doping, the virtual level acquires dispersion but now according to the scenario described above and it is detected in ARPES experiments. The existence of an energy pseudogap is based on the difference in the dispersion laws between the valence and narrow impurity bands. Comparing the computed dispersion curves with the ARPES observations [40] we conclude that dispersion, characteristic for the para phase in all experimental samples, is observed in the experiment along the direction $\Gamma \longleftrightarrow \overline{M}$, while near X a similar dispersion is observed only for an optimally doped sample. The appearance of an energy gap near X is a consequence of the manifestation of an impurity band near energies above the Fermi energy with doping of antiferromagnetic CuO_2 layer. Our conclusions, just as the conclusions of [44], do not support the conclusions of [19] that it is impossible to describe in a unified approach the dispersion relations for an antiferromagnetic dielectric and doped samples.

Calculation of the evolution of the Fermi surface taking doping into account requires a self-consistent calculation of the Fermi level for each hole density. Since the band structure itself depends on the density and cannot be described by a rigid-band model, this problem requires a large volume of calculations and falls outside the scope of the present paper.

ACKNOWLEDGMENT

This work was supported by the Krasnoyarsk Krai Science Foundation (project no. 8F0032).

REFERENCES

1. P. W. Anderson, Science **235**, 196 (1987); R. O. Zaĭtsev and V. A. Ivanov, Fiz. Tverd. Tela (Leningrad) **29**, 2554 (1987) [Sov. Phys. Solid State **29**, 1475 (1987)].
2. P. Kuiper, G. Kruizinga, J. Chijsen, *et al.*, Phys. Rev. B **38**, 6483 (1988).
3. N. Nucker, J. Fink, J. C. Fugle, *et al.*, Phys. Rev. Lett. **58**, 2794 (1987).
4. V. J. Emery, Phys. Rev. Lett. **58**, 2794 (1987).
5. C. M. Varma, S. Schmitt-Rink, and E. Abrahams, Solid State Commun. **62**, 681 (1987).
6. Yu. B. Gaididei and V. M. Loktev, Phys. Status Solidi B **147**, 307 (1988).
7. F. C. Zhang and T. M. Rice, Phys. Rev. B **37**, 3759 (1988).
8. H. Eskes and J. H. Jefferson, Phys. Rev. B **48**, 9788 (1993).
9. H. Eskes and G. A. Sawatzky, Phys. Rev. Lett. **61**, 1415 (1988).
10. E. B. Stechel and D. R. Jennison, Phys. Rev. B **38**, 4632 (1988).
11. H. Eskes, G. A. Savatzky, and L. F. Feiner, Physica C (Amsterdam) **160**, 424 (1989).
12. J. H. Jefferson, H. Eskes, and L. F. Feiner, Phys. Rev. B **45**, 7959 (1992).
13. S. V. Lovtsov and V. Yu. Yushankhai, Physica C (Amsterdam) **179**, 159 (1991).
14. H.-B. Schutler and A. J. Fedro, Phys. Rev. B **45**, 7588 (1992).
15. S. G. Ovchinnikov and I. S. Sandalov, Physica C (Amsterdam) **198**, 607 (1989).
16. J. H. Jefferson, Physica B (Amsterdam) **165–166**, 1013 (1990).
17. V. I. Belinicher, A. L. Chernyshev, and V. A. Shubin, Phys. Rev. B **53**, 335 (1996).
18. A. Nazarenko, K. J. E. Vos, S. Haas, *et al.*, Phys. Rev. B **51**, 8676 (1995).
19. D. Daffy, A. Nazarenko, S. Haas, *et al.*, Phys. Rev. B **56**, 5597 (1997).
20. B. O. Wells, Z.-X. Shen, A. Matsuura, *et al.*, Phys. Rev. Lett. **74**, 964 (1995).
21. A. Bianconi *et al.*, Physica C (Amsterdam) **162–164**, 209 (1989).
22. H. Romberg *et al.*, Phys. Rev. B **41**, 2609 (1990).

23. L. F. Feiner, J. H. Jefferson, and R. Raimondi, Phys. Rev. B **53**, 8751 (1996).
24. R. Raimondi, J. H. Jeferson, and L. F. Feiner, Phys. Rev. B **53**, 8774 (1996).
25. S. G. Ovchinnikov, Phys. Rev. B **49**, 9891 (1994).
26. C. G. Ovchinnikov, Zh. Éksp. Teor. Fiz. **107**, 796 (1995) [JETP **80**, 451 (1995)].
27. S. G. Ovchinnikov, Zh. Éksp. Teor. Fiz. **102**, 534 (1992) [Sov. Phys. JETP **75**, 283 (1992)].
28. S. G. Ovchinnikov, Pis'ma Zh. Éksp. Teor. Fiz. **64**, 23 (1996) [JETP Lett. **64**, 25 (1996)].
29. B. S. Shastry, Phys. Rev. Lett. **63**, 1288 (1989).
30. R. O. Zaĭtsev, Zh. Éksp. Teor. Fiz. **68** (1), 207 (1975) [Sov. Phys. JETP **41**, 100 (1975)].
31. V. A. Gavrichkov, M. Sh. Erukhimov, S. G. Ovchinnikov, and I. S. Édel'man, Zh. Éksp. Teor. Fiz. **90**, 1275 (1986) [Sov. Phys. JETP **63**, 744 (1986)].
32. Z. Liu and E. Manousakis, Phys. Rev. B **45**, 2425 (1992).
33. O. K. Andersen, A. Liechtenstein, O. Jepsen, and F. Paulsen, J. Phys. Chem. Solids **56**, 1573 (1995).
34. G. Martinez and P. Horsch, Phys. Rev. B **44**, 317 (1991).
35. E. Daggotto, F. Ortolani, and D. Scalapino, Phys. Rev. B **46**, 3183 (1992).
36. G. Khaliullin and P. Horsch, Phys. Rev. B **47**, 463 (1993).
37. G. G. Khaliullin, Pis'ma Zh. Éksp. Teor. Fiz. **52**, 999 (1990) [JETP Lett. **52**, 389 (1990)].
38. J. L. Richard and V. Yu. Yushankhai, Phys. Rev. B **50**, 12927 (1994).
39. S. G. Ovchinnikov, Usp. Fiz. Nauk **167**, 1043 (1997) [Phys. Usp. **40**, 993 (1997)].
40. M. Guptasarma, D. G. Hinks, and M. V. Klein, Phys. Rev. Lett. **82**, 5349 (1999).
41. D. S. Marshall *et al.*, Phys. Rev. Lett. **76**, 4841 (1996).
42. P. Prelovsek, J. Jaklic, and K. Bedell, Phys. Rev. B **60**, 40 (1999).
43. A. P. Kampf and J. R. Schrieffer, Phys. Rev. B **41**, 6399 (1990).
44. J. Schmalian, D. Pains, and B. Stoykovich, Phys. Rev. B **60**, 667 (1999).

Translation was provided by AIP